

ISO Spectroscopy of the young bipolar nebulae S106 IR and Cep A East*

M.E. van den Ancker^{1,2}, A.G.G.M. Tielens^{3,4,5}, and P.R. Wesselius⁴

¹ Astronomical Institute “Anton Pannekoek”, University of Amsterdam, Kruislaan 403, 1098 SJ Amsterdam, The Netherlands

² Harvard-Smithsonian Center for Astrophysics, 60 Garden Street, MS 42, Cambridge, MA 02138, USA

³ Kapteyn Astronomical Institute, Groningen University, P.O. Box 800, 9700 AV Groningen, The Netherlands

⁴ SRON, P.O. Box 800, 9700 AV Groningen, The Netherlands

⁵ NASA Ames Research Center, MS 245-3, Moffett Field, CA 94035, USA

Received 23 February 2000 / Accepted 2 May 2000

Abstract. We present the results of ISO SWS and LWS grating scans towards the embedded Young Stellar Objects (YSOs) S106 IR and Cep A East. Emission from the pure rotational lines of H₂ and the infrared fine structure lines of [C II], [O I], [S I], [Si II] and [Fe II], as well as absorption bands due to H₂O, CO and CO₂ ice were detected toward Cep A. In S106 we detected emission lines of H₂, CO, H I, and a large number of ionized species including Fe, O, N, C, Si, S, Ne and Ar. S106 also shows many of the infrared PAH bands in emission. Excitation temperatures and molecular hydrogen masses were derived from the low-lying pure rotational levels of H₂ and are 500 and 730 K and 8 and $3 \times 10^{-3} M_{\odot}$ for S106 and Cep A, respectively. Since both objects are expected to have several solar masses of H₂ in their environment, we conclude that in both cases the bulk of the H₂ is cooler than a few hundred Kelvins. Excitation temperatures and line ratios were compared with those predicted by theoretical models for PDRs and dissociative and non-dissociative shocks. The [S I] 25.2 μm /[Si II] 34.8 μm ratio is a particularly useful shock versus PDR discriminant and we conclude that S106 IR is dominated by PDR emission while Cep A East has a large shock component. From an analysis of the ionic lines in S106 we conclude that the central star must have a temperature around 37,000 K, corresponding to a spectral type of O8. From its luminosity it is concluded that the driving source of Cep A must also be a massive early-type star. The absence of strong high-ionization ionic lines in its ISO spectrum shows that Cep A has not yet created a significant H II region and must be younger than S106, illustrating the process of the clearing of the surroundings of a massive young star.

Key words: shock waves – stars: circumstellar matter – stars: formation – ISM: H II regions – ISM: jets and outflows – infrared: stars

Send offprint requests to: M.E. van den Ancker (mario@astro.uva.nl)

* Based on observations with ISO, an ESA project with instruments funded by ESA Member States (especially the PI countries: France, Germany, the Netherlands and the United Kingdom) and with the participation of ISAS and NASA.

1. Introduction

The infrared emission-line spectrum of a Young Stellar Object (YSO) is dominated by the interaction of the central star with the remnants of the clouds from which it formed. The intense UV radiation generated by accretion as well as by the central star itself causes dissociation of molecular material close to the YSO and ionizes much of the atomic material, giving rise to typical nebular and recombination lines. Furthermore, the interaction of the UV field with the remnants of the star’s natal cloud will produce a photodissociation region (PDR; see Hollenbach & Tielens 1999 for a comprehensive review). In a PDR, heating of the gas occurs by collisions with electrons, photoelectrically ejected from grain surfaces. The gas in the surface regions of PDRs reaches temperatures of typically 500 K (e.g. Tielens & Hollenbach 1985), producing a distinctive infrared spectrum due to collisionally excited low-lying levels of many molecular and neutral species.

Another phenomenon associated with YSOs are strong stellar winds, often collimated into a bipolar outflow. These will cause a shock as they drive a supersonic wave into the surrounding molecular cloud, heating it in the process. Shocks are usually divided into two distinct categories: J- or Jump-shocks, and C- or Continuous-shocks. In J-shocks viscous heating of the neutrals occurs in a thin shock front in which radiative cooling is insignificant, while the post-shock gas is heated to several times 10^4 degrees, dissociating all molecular material (e.g. Hollenbach & McKee 1989). Cooling of the post-shock gas occurs through atomic fine-structure lines as well as through reformation of molecules. In contrast, C-shocks are magnetized, non-dissociative shocks in which the physical conditions change more gradually from their pre- to post-shock values and cooling is mainly through radiation from molecular material (e.g. Kaufman & Neufeld 1996). If the temperatures in a C-shock become sufficiently high to start to dissociate molecules, the cooling through the molecular lines diminishes, and the shock temperature increases until it turns into a J-shock. Shocks with a shock velocity larger than 40 km s^{-1} are usually J-shocks, whereas slower shocks are usually of C-type (Chernoff et al.

1982). In this paper we will illustrate the power of infrared spectroscopy to study the above mentioned phenomena using two young bipolar nebulae, S106 and Cep A.

The bipolar nebula S106 is one of the most studied H II regions in our galaxy. The exciting source of the region is a very young massive stellar object, known as either IRS4 in the terminology of Gehrz et al. (1982) or IRS3 following Pipher et al. (1976). Around this central source, Hodapp & Rayner (1991) found a cluster of about 160 stars, embedded in the molecular cloud surrounding S106. Observed radio emission and H I recombination lines from the region have been suggested to arise in a strong ($\dot{M} \approx 2 \times 10^{-5} M_{\odot} \text{ yr}^{-1}$), fast ($\approx 200 \text{ km s}^{-1}$), stellar wind, driving a shock into the surrounding extended molecular cloud (Hippelein & Münch 1981). A dark lane, largely devoid of any optical or infrared emission, separates the two lobes of the H II region. This dark lane has been quoted many times as a prime example of a large ($30''$) circumstellar disk, consisting of cool gas and dust, seen nearly edge-on (Bieging 1984; Mezger et al. 1987). However, Loushin et al. (1990) showed this structure to be an expanding ring of molecular material rather than a protoplanetary disk. Near-infrared ro-vibrational emission of H₂ is seen to arise just outside the H II region, suggesting an origin in a PDR (Hayashi et al. 1990).

Cep A is another well-known site of recent star formation. It contains a luminous ($2.5 \times 10^4 L_{\odot}$; Evans et al. 1981) far-infrared source, as well as several fainter infrared sources. The core of the Cep A region remains obscured at optical and infrared wavelengths due to massive amounts of extinction, and is the source of an energetic, complex molecular outflow (Bally & Lane 1982). Radio-observations show that it contains two strings of about 13 ultracompact H II regions, arranged in a Y-shape (Hughes 1988). The source IRS 6a (Lenzen et al. 1984), located in the infrared nebula to the east of the core, is the dominant source of the eastern lobe at $20 \mu\text{m}$ (Ellis et al. 1990), but polarization measurements show that the nebula is illuminated by the compact radio source HW-2 (Hughes & Wouterloot 1984), located $\sim 5''$ south of IRS 6a (Casement & McLean 1996). The fact that it is not visible at $20 \mu\text{m}$ implies an extremely large extinction towards HW-2. H₂ emission occurs in both the eastern and western parts of the nebula (Doyon & Nadeau 1988). Hartigan et al. (1996) showed that the molecular emission to the east appears as a regular jet, whereas that to the west concentrates in shells, which they proposed to arise in wakes from bow shocks surrounding Herbig-Haro objects in the region. ISO observations of the western part of the region were discussed by Wright et al. (1996), who modelled the observed infrared fine structure lines as arising in a planar J-shock with shock velocity $70\text{--}80 \text{ km s}^{-1}$. The same authors modelled the observed molecular hydrogen emission as arising in a combination of several C-shocks. This multitude of shocks in the region agrees with the explanation of Narayanan & Walker (1996), who reported the presence of multiple episodes of outflow activity from the region. Recently, Goetz et al. (1998) presented strong evidence for this scenario through near-infrared H₂ and [Fe II] images of Cep A East showing several distinct regions containing shocks.

In this paper we will present new *Infrared Space Observatory* (ISO; Kessler et al. 1996) data on infrared fine-structure and molecular emission lines from the central region of S106, centered on IRS4, and the eastern part of Cep A, centered on IRS 6a. These data give for the first time access to a large spectral range that was unaccessible from ground-based observations and contain lines which are decisive probes of the excitation conditions. We will show that the observed emission-line spectrum can be well explained as arising in the combination of a PDR and a H II region in the case of S106, whereas this emission is shock-excited in the case of Cep A.

2. Observations and data

ISO Short Wavelength (2.4–45 μm) Spectrometer (SWS; de Graauw et al. 1996) full grating scans (“AOT S01”) of S106 IR and Cep A East were obtained in ISO revolutions 335 (JD 2450373.740) and 843 (JD 2450880.050), respectively. Each of these observations took 2124 seconds of observing time. In addition to this, deeper SWS grating scans on selected molecular and fine transition lines in the two objects (“AOT S02”) were obtained in revolutions 134 (at JD 2450172.705; S106), 220 (JD 2450258.463; Cep A) and 566 (JD 2450603.706; Cep A). In revolutions 558 (JD 2450596.103) and 580 (JD 2450617.838), scans at the full SWS grating resolution (“AOT S06”) covering the wavelength ranges of 3.0–3.5, 4.0–6.8, 7.0–7.6 and 12.1–16.5 μm were obtained for S106 as well. ISO Long Wavelength (43–197 μm) Spectrometer (LWS; Clegg et al. 1996) grating scans (“AOT L01”) of S106 IR and Cep A East were obtained in revolutions 134 (JD 2450172.726) and 566 (JD 2450603.681), respectively. Data were reduced in a standard fashion using calibration files corresponding to OLP version 7.0, after which they were corrected for remaining fringing and glitches. To increase the S/N in the final spectra, the detectors were aligned and statistical outliers were removed, after which the spectra were rebinned to a lower spectral resolution.

The SWS full grating scans consist of twelve different grating scans, each covering a small wavelength region, which were joined to form one single spectrum. Because of the variation of the diffraction limit of the telescope with wavelength, different SWS bands use apertures of different sizes. This is illustrated in Figs. 1 and 2, where we show their relative position and size, overlaid on K-band (2.2 μm) images of S106 and Cep A East by Hodapp & Rayner (1991) and Hodapp (1994). For a source that is not point-like, one may see a discontinuity in the spectra at the wavelengths where a change in aperture occurs, which can indeed be seen in both the S106 and Cep A spectra. The relative discontinuities in S106 are close to the maximum possible values, indicating that the source is extended across the entire SWS aperture at the longer wavelengths ($33'' \times 20''$). In Cep A the discontinuities are smaller, pointing to a smaller size of the far-infrared source.

Since both spectrometers on board ISO use entrance apertures that are smaller than the beam size, a wavelength dependent correction has to be applied to the standard flux calibration when observing extended sources. We determined these correc-

Table 1. Observed and extinction-corrected line fluxes for S106 IR and Cep A East (in 10^{-15} W m $^{-2}$). Also listed are predicted line fluxes from the H II + PDR model (S106 IR) and the shock model (Cep A) discussed in the text.

Line	λ [μ m]	Beam [10^{-8} sr]	S106 IR				Cep A East			
			AOT	Observed	Ext. corr.	Model	AOT	Observed	Ext. Corr.	Model
H ₂ 0–0 S(0)	28.2188	1.64	S02	< 1.58	< 1.67	0.03	S02	< 3.62	< 3.69	0.03
H ₂ 0–0 S(1)	17.0348	1.15	S02	0.58±0.18	0.75±0.23	0.98	S02	0.27±0.10	0.28±0.11	0.54
H ₂ 0–0 S(2)	12.2786	1.15	S02	1.18±0.49	1.61±0.66	0.97	S02	1.27±0.64	1.33±0.67	1.32
H ₂ 0–0 S(3)	9.6649	0.85	S02	1.19±0.52	2.55±1.11	2.01	S02	0.90±0.38	1.01±0.43	1.31
H ₂ 0–0 S(4)	8.0251	0.85	S02	0.82±0.29	1.05±0.37	0.76	S02	1.33±0.33	1.38±0.34	1.02
H ₂ 0–0 S(5)	6.9095	0.85	S02	1.47±0.73	1.69±0.85	0.82	S02	2.42±0.43	2.47±0.43	2.98
H ₂ 0–0 S(6)	6.1086	0.85	S02	< 1.60	< 1.89	0.04	S02	0.84±0.32	0.86±0.32	0.20
H ₂ 0–0 S(7)	5.5112	0.85	S02	0.94±0.47	1.13±0.56	0.02	S02	2.48±0.62	2.55±0.63	0.08
H ₂ 0–0 S(8)	5.0531	0.85	S06	< 0.29	< 0.36	0.00	S02	0.46±0.13	0.48±0.13	0.01
H ₂ 0–0 S(9)	4.6946	0.85	S02	< 0.57	< 0.73	0.00	S02	< 1.17	< 1.21	0.00
H ₂ 0–0 S(10)	4.4099	0.85	S02	< 0.48	< 0.62	0.00	S02	0.98±0.49	1.02±0.51	0.00
H ₂ 0–0 S(11)	4.1813	0.85	S02	< 0.77	< 1.03	0.00	S02	< 0.64	< 0.67	0.00
H ₂ 0–0 S(12)	3.9960	0.85	S02	< 0.28	< 0.38	0.00	S02	< 0.78	< 0.82	0.00
H ₂ 1–0 O(5)	3.2350	0.85	S06	0.30±0.05	0.46±0.07	0.00	S01	< 0.74	< 0.79	0.00
H I H7 α	19.0624	1.15	S02	0.89±0.30	1.18±0.40	–	S02	< 0.28	< 0.29	–
H I H7 β	11.3090	0.85	S02	0.83±0.32	1.29±0.50	–	S01	< 1.05	< 1.12	–
H I H7 γ	8.7603	0.85	S02	0.92±0.30	1.57±0.50	–	S01	< 0.70	< 0.76	–
H I H7 ϵ	6.7720	0.85	S06	0.87±0.43	1.01±0.50	–	S01	< 3.67	< 3.75	–
H I H7 13	6.2919	0.85	S06	< 3.25	< 3.80	–	S01	< 3.05	< 3.12	–
H I H7 14	5.9568	0.85	S06	0.54±0.17	0.64±0.20	–	S01	< 4.28	< 4.39	–
H I Hu α	12.3719	1.15	S06	4.69±1.31	6.33±1.77	–	S01	< 6.30	< 6.58	–
H I Hu β + H7 δ	7.5083	0.85	S02	4.99±1.74	5.79±2.01	–	S02	< 1.37	< 1.40	–
H I Hu γ	5.9082	0.85	S06	3.08±0.52	3.67±0.62	–	S01	< 2.94	< 3.01	–
H I Hu δ	5.1287	0.85	S06	2.60±0.41	3.20±0.51	–	S01	< 1.91	< 1.96	–
H I Hu ϵ	4.6725	0.85	S06	0.87±0.26	1.10±0.33	–	S01	< 6.53	< 6.76	–
H I Hu 12	4.3765	0.85	S06	1.08±0.33	1.40±0.43	–	S01	< 2.01	< 2.09	–
H I Hu 13	4.1708	0.85	S06	1.54±0.51	2.05±0.67	–	S01	< 9.77	< 10.2	–
H I Hu 14	4.0210	0.85	S02	0.97±0.10	1.32±0.14	–	S01	< 1.45	< 1.51	–
H I Pf α	7.4600	0.85	S02	14.6±3.6	16.8±4.2	–	S02	< 0.30	< 0.31	–
H I Pf β	4.6539	0.85	S02	9.21±1.18	11.7±1.5	–	S01	< 4.93	< 5.11	–
H I Pf γ	3.7406	0.85	S02	5.60±0.58	7.90±0.82	–	S01	< 1.45	< 1.52	–
H I Pf δ	3.2970	0.85	S02	3.45±0.28	5.32±0.43	–	S01	< 0.72	< 0.76	–
H I Pf ϵ	3.0393	0.85	S06	2.87±0.36	4.76±0.60	–	S01	< 0.65	< 0.70	–
H I Br α	4.0523	0.85	S02	44.6±3.7	60.4±5.0	–	S02	< 1.42	< 1.48	–
H I Br β	2.6259	0.85	S01	16.9±1.2	32.7±2.3	–	S02	< 1.09	< 1.20	–
CO $J=14-13$	185.999	12.2	L01	118.4±39.5	119.0±39.7	128.0	L01	28.3±2.0	28.3±2.0	29.1
CO $J=15-14$	173.631	12.2	L01	191.3±63.8	192.5±64.2	149.9	L01	28.3±2.0	28.3±2.0	26.5
CO $J=16-15$	162.812	11.6	L01	96.4±32.1	97.0±32.3	122.5	L01	21.1±1.5	21.1±1.5	22.7
CO $J=17-16$	153.267	11.6	L01	99.8±33.3	100.5±33.5	98.4	L01	< 33.3	< 33.4	19.7
He I ($^3D_1-^3F_0$)	4.0373	0.85	S02	1.42±0.28	1.93±0.38	–	S02	< 2.05	< 2.15	–
He I ($^3S_1-^3P_0$)	4.2954	0.85	S06	6.43±0.85	8.45±1.12	–	S01	< 6.91	< 7.19	–
[Ca IV] ($^2P_{3/2}-^2P_{1/2}$)	3.2067	0.85	S06	0.26±0.05	0.40±0.08	0.00	S01	< 0.68	< 0.72	0.00
[Fe I] ($^5D_4-^5D_3$)	24.0424	1.15	S02	< 1.01	< 1.22	0.05	S02	< 1.19	< 1.23	–
[Fe I] ($^5D_3-^5D_2$)	34.7135	2.01	S02	< 5.99	< 6.64	0.02	S02	< 4.74	< 4.81	–
[Fe II] ($^6D_{9/2}-^4F_{9/2}$)	5.3403	0.85	S06	3.04±0.60	3.69±0.73	–	S01	< 4.14	< 4.26	–
[Fe II] ($^4F_{9/2}-^4F_{7/2}$)	17.9363	1.15	S02	0.89±0.26	1.19±0.35	0.97	S02	0.24±0.06	0.25±0.07	0.23
[Fe II] ($^6D_{9/2}-^6D_{7/2}$)	25.9882	1.15	S02	5.27±1.10	6.20±1.29	3.37	S02	0.64±0.21	0.66±0.21	0.98
[Fe II] ($^6D_{7/2}-^6D_{5/2}$)	35.3491	2.01	S02	4.94±2.47	5.46±2.73	1.21	S02	< 4.01	< 4.07	0.40
[Fe III] ($^5D_4-^5D_3$)	22.9250	1.15	S01	19.2±3.9	23.5±4.7	28.0	S01	< 22.7	< 23.4	0.00
[Ni II] ($^2D_{5/2}-^2D_{3/2}$)	6.6360	0.85	S06	1.88±0.42	2.19±0.49	1.32	S01	< 3.04	< 3.11	1.43
[Ni III] ($^3F_4-^3F_3$)	7.349	0.85	S06	1.33±0.35	1.53±0.41	1.05	S01	< 0.66	< 0.67	0.00
[Ar II] ($^2P_{3/2}-^2P_{1/2}$)	6.9853	0.85	S01	64.4±9.7	74.2±11.2	74.2	S01	< 1.19	< 1.22	–
[Ar III] ($^3P_2-^3P_1$)	8.9914	0.85	S01	24.0±6.0	44.3±11.1	44.5	S01	< 1.11	< 1.22	0.00
[Ne II] ($^2P_{3/2}-^2P_{1/2}$)	12.8135	1.15	S06	239.6±60.1	309.3±77.5	320.2	S01	< 2.80	< 2.91	2.67

Table 1. (continued)

Line	λ [μm]	Beam [10^{-8} sr]	S106 IR				Cep A East			
			AOT	Observed	Ext. corr.	Model	AOT	Observed	Ext. Corr.	Model
[Ne III] ($^3P_2-^3P_1$)	15.5551	1.15	S06	31.4 \pm 7.9	39.3 \pm 9.9	31.7	S01	7.87 \pm 2.01	8.13 \pm 2.17	0.00
[S I] ($^3P_2-^3P_1$)	25.2490	1.15	S02	< 2.96	< 3.52	0.05	S02	0.70 \pm 0.21	0.72 \pm 0.22	0.82
[S III] ($^3P_1-^3P_2$)	18.7130	1.15	S01	169.4 \pm 34.0	225.3 \pm 45.2	243.1	S01	< 2.80	< 2.92	0.00
[S III] ($^3P_0-^3P_1$)	33.4810	2.01	S01	132.9 \pm 19.3	148.2 \pm 21.5	155.5	S01	< 39.2	< 39.9	0.00
[S IV] ($^2P_{1/2}-^2P_{3/2}$)	10.5105	0.85	S01	7.33 \pm 1.85	13.47 \pm 3.40	14.6	S01	< 1.07	< 1.16	0.00
[Si II] ($^2P_{1/2}-^2P_{3/2}$)	34.8152	2.01	S02	152.3 \pm 59.2	168.7 \pm 65.6	116.9	S02	5.86 \pm 0.22	5.94 \pm 0.23	4.21
[N III] ($^2P_{1/2}-^2P_{3/2}$)	57.34	15.7	L01	98.7 \pm 19.8	103.4 \pm 20.8	88.4	L01	< 81.0	< 81.6	0.00
[O I] ($^3P_2-^3P_1$)	63.1850	16.3	L01	1125 \pm 114	1172 \pm 118	1131	L01	201.9 \pm 11.1	203.1 \pm 14.2	116.1
[O I] ($^3P_1-^3P_0$)	145.535	8.82	L01	288.8 \pm 29.0	291.2 \pm 29.2	320.6	L01	14.4 \pm 1.8	14.4 \pm 1.8	2.49
[O III] ($^3P_1-^3P_2$)	51.8145	15.7	L01	381.4 \pm 42.8	403.8 \pm 45.3	388.5	L01	< 80.9	< 81.5	0.00
[O III] ($^3P_0-^3P_1$)	88.3562	14.8	L01	124.9 \pm 15.1	127.5 \pm 15.4	112.9	L01	< 50.3	< 50.5	0.00
[C II] ($^2P_{1/2}-^2P_{3/2}$)	157.741	11.6	L01	157.2 \pm 15.9	158.3 \pm 16.0	140.3	L01	16.3 \pm 2.0	16.4 \pm 2.0	2.66

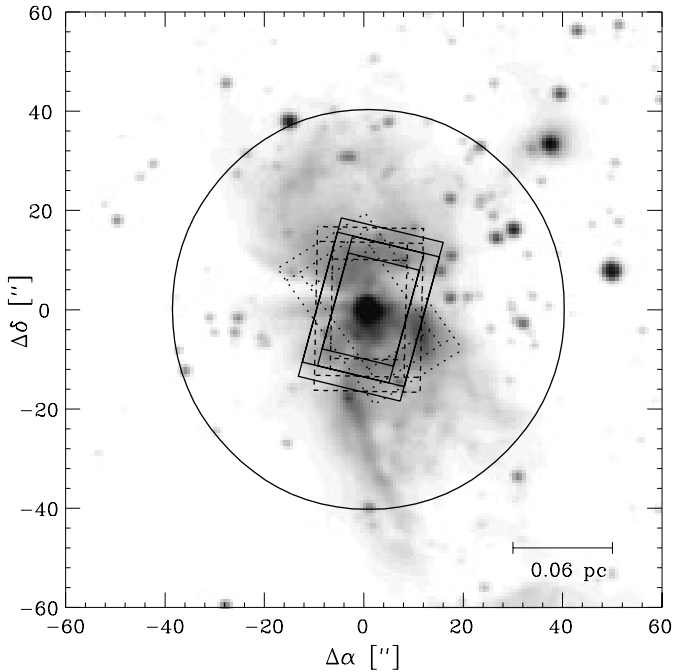


Fig. 1. SWS AOT S01 (solid rectangles), AOT S02 (dashed rectangles), AOT S06 (dotted rectangles) and LWS (solid circle; beam average FWHM) aperture positions for our measurements of S106 superimposed on a K'-band image of the region. The rectangles indicate the apertures (in increasing size) for SWS bands 1A–2C (2.4–12.0 μm), 3A–3D (12.0–27.5 μm), 3E (27.5–29.5 μm) and 4 (29.5–40.5 μm).

tion factors by convolving the K-band images of S106 and Cep A East, with the beam profile and applied these to the data before further analysis. The maximum correction to the flux was 8% in the region around 40 μm . If the sources are more extended at the longer wavelengths or in specific lines than the K-band images we employed in estimating the diffraction losses, we will have underestimated the flux. The maximum error this could introduce in the flux calibration is $\approx 15\%$.

Figs. 3 and 4 show the resulting SWS and LWS full grating scans for S106 IR and Cep A East. Scanned lines and measured

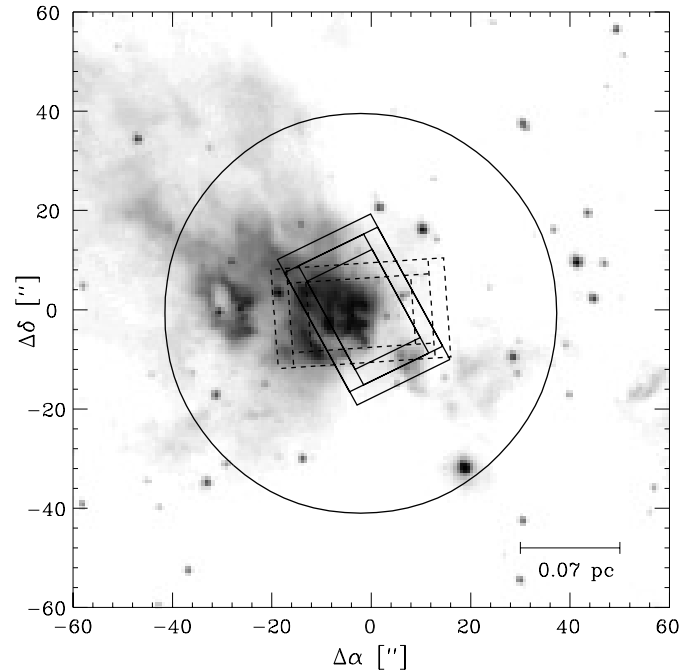


Fig. 2. Same as Fig. 1 for Cep A East.

line fluxes or upper limits (total flux for line with peak flux 3σ) are listed in Table 1. The errors listed in Table 1 include the errors in the absolute flux calibration; errors in line ratios used in the remainder of this paper may be lower. Plots of all detected lines, rebinned to a resolution $\lambda/\Delta\lambda$ of 1500 with an oversampling factor of four (SWS), or to a resolution of 500 (LWS), are given in Figs. 5 and 6. In the same figures we also show the line profiles expected for an unresolved point-source and an unresolved extended source filling the entire aperture. All detected lines in both S106 and Cep A are compatible with these profiles. For lines measured with the full SWS grating resolution (AOT S02 or S06), this indicates that they have a FWHM of less than $\approx 150 \text{ km s}^{-1}$.

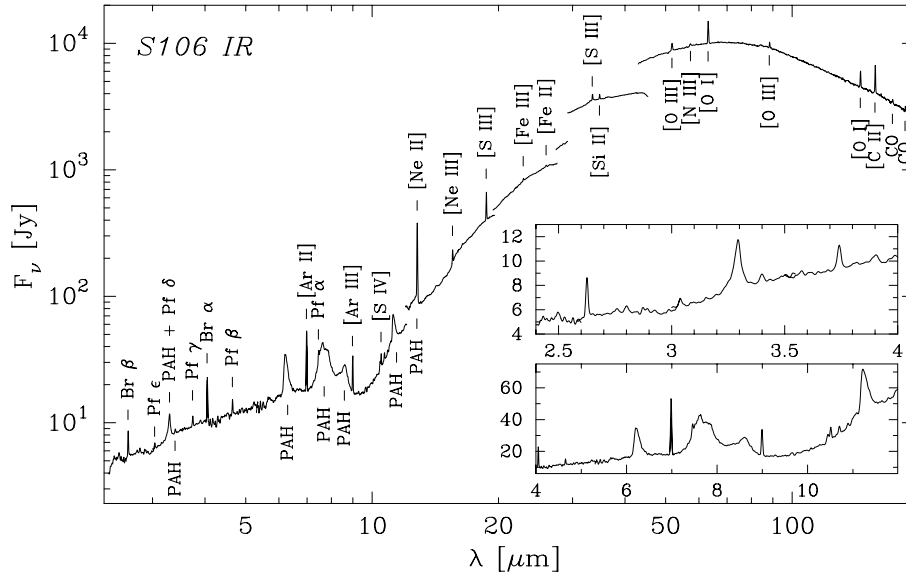


Fig. 3. Combined ISO SWS/LWS full grating spectrum for S106 IR with the most prominent features identified. The insets show enlargements of the SWS spectrum in the 2.4–4.0 and 4.0–12.0 micron range.

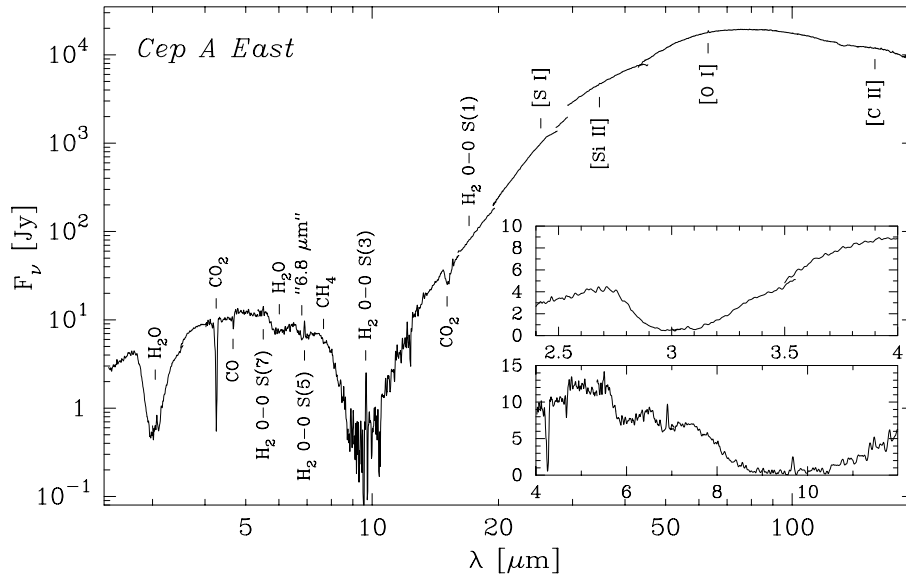


Fig. 4. Same as Fig. 3 for Cep A East.

Table 2. Column densities of solid state absorption features towards S106 and Cep A.

Species	λ [μm]	A_m [cm molec^{-1}]	Cep A East		S106 IR	
			$\int \tau(\nu) d\nu$ [cm^{-1}]	N [cm^{-2}]	$\int \tau(\nu) d\nu$ [cm^{-1}]	N [cm^{-2}]
H ₂ O	3.0	2.0×10^{-16}	1051	5.3×10^{18}	10.1	5.1×10^{16}
H ₂ O	6.0	1.2×10^{-17}	60	5.0×10^{18}	< 4.9	< 4.1×10^{17}
CO	4.67	1.1×10^{-17}	3.8	3.5×10^{17}	< 1.9	< 1.7×10^{17}
CO ₂	4.26	7.6×10^{-17}	58	7.6×10^{17}	< 6.4	< 8.4×10^{16}
CO ₂	15.2	1.1×10^{-17}	9.2	8.4×10^{17}	< 1.5	< 1.3×10^{17}
CH ₄	7.67	7.3×10^{-18}	1.7	2.3×10^{17}	< 2.8	< 3.9×10^{17}
Silicate	9.7	1.2×10^{-16}	965	8.0×10^{18}	106	8.8×10^{17}

3. Solid-state features

The SWS spectrum of S106 (Fig. 3) consists of a relatively smooth continuum, with numerous strong emission lines superimposed. The continuum appears to consist of two components,

with the break between the two occurring around 10 μm . This is similar to the situation seen in other regions of recent star formation, where these two components are commonly ascribed to emission due to dust close to the star (2–10 μm) and small dust

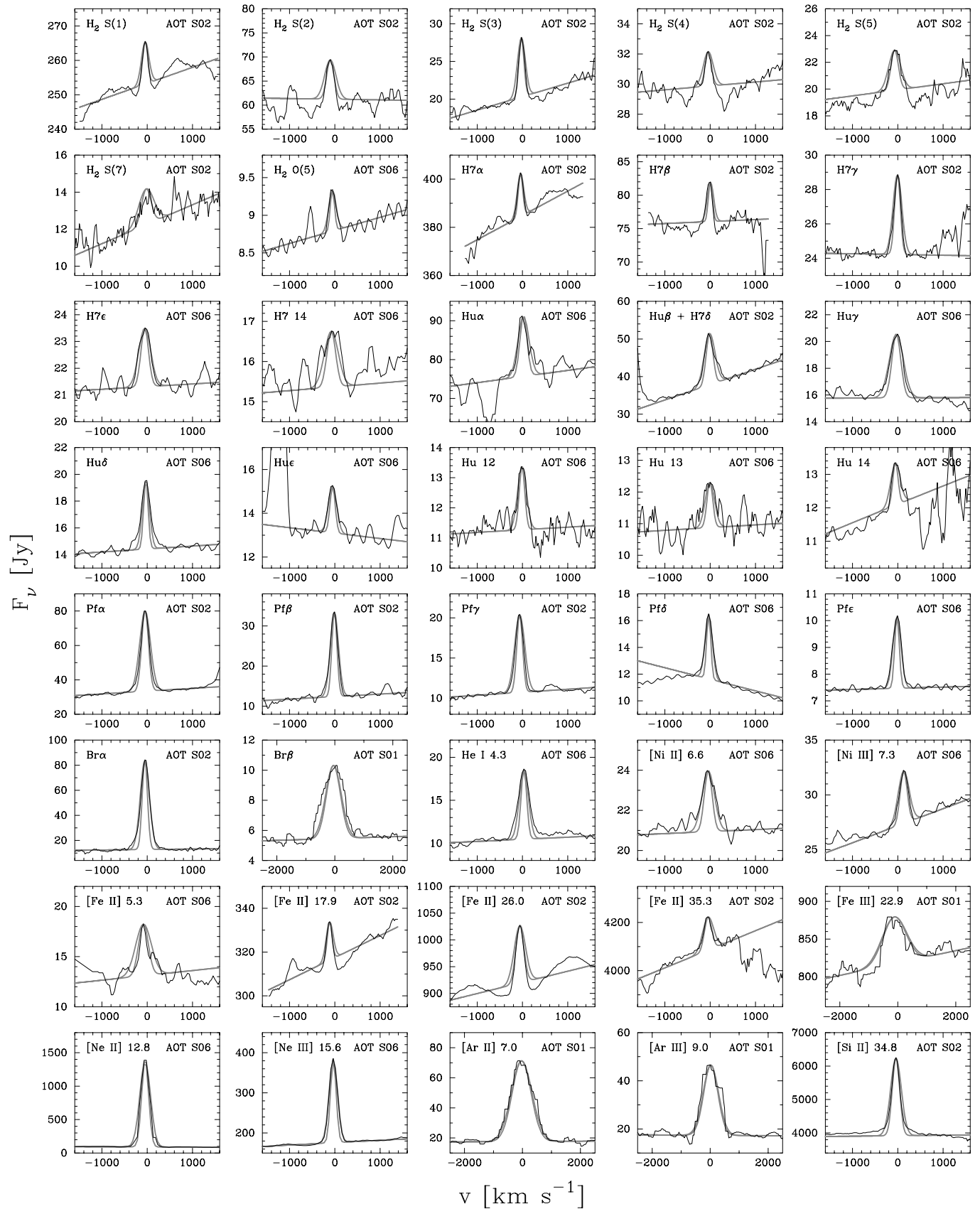


Fig. 5. Detected lines in S106 IR. The velocities are heliocentric. The grey lines show the instrumental profiles for a point source (narrower profile) and an extended source (wide profile) filling the entire aperture.

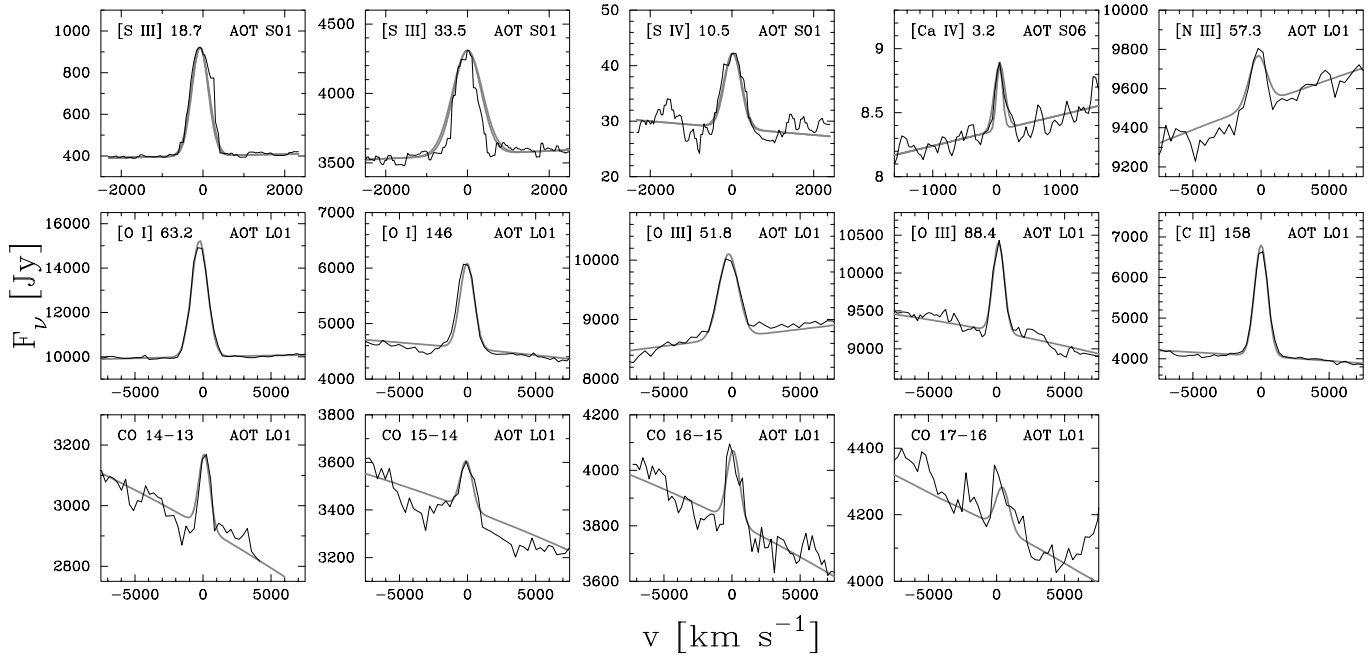


Fig. 5. (continued)

grains in the wide circumstellar environment (10–200 μm ; e.g. Cesarsky et al. 1996).

The familiar UIR bands at 3.3, 3.4, 6.2, 7.6, 7.8, 8.6, 11.3 and 12.7 μm , usually attributed to polycyclic aromatic hydrocarbons (PAHs), are present in emission and strong. As first demonstrated by ground-based spatially resolved CVF spectroscopy of the 3.3 μm band by Felli et al. (1984), these features do not come from the central point-source IRS4, but originate in the wide circumstellar environment. The band-strengths of the UIR features in our ISO spectra appear consistent with the ground-based measurements present in literature (Hefele & Hölzle 1980; Felli et al. 1984; Geballe et al. 1985).

An absorption band around 3.0 μm due to the O–H stretch mode of H_2O ice, previously undetected in S106, is present in the SWS spectrum. Although partly filled in by emission from the 7.6, 7.8, 8.6 and 11.3 μm UIR bands, a 9.7 μm absorption feature due to the Si–O stretching mode in amorphous silicates also appears present in Fig. 3. The combination of the contamination by the UIR bands and the limited baseline can explain why this feature has not been detected from the ground. A weak dip around 18–19 μm in our ISO data may be identified with the Si–O bending mode of amorphous silicate, confirming the presence of silicate absorption in S106.

Since extinction in the continuum surrounding the 9.7 μm feature is small compared to the extinction within this feature, the extinction A_λ at wavelength λ across a non-saturated 9.7 μm feature can simply be obtained from the relation $A_\lambda = -2.5 \log(I/I_0)$. Using an average interstellar extinction law which includes the silicate feature (Fluks et al. 1994), we can then convert these values of A_λ to a visual extinction, resulting in a value of $A_V = 13^{m.7}$ toward S106 IR. This value is in excellent agreement with that of $13^{m.4} \pm 2.7$, derived towards

stars in the S106 embedded cluster (Hodapp & Rayner 1991), or the value of $15^{m.} \pm 3^{m.}$ predicted from infrared H I lines by Alonso-Kosta & Kwan (1989). It is also in agreement with the extinction of $A_V = 12^{m.}$ towards the northern lobe of the S106 nebula (Felli et al. 1984). It is somewhat larger than that towards the southern lobe ($A_V = 8^{m.}$; Felli et al. 1984) and much smaller than that towards the central source ($A_V = 21^{m.}$; Eiroa et al. 1979).

For Cep A East the SWS spectrum (Fig. 4) is dominated by absorption bands from a variety of ices. The O–H bend and stretch modes of H_2O at 3.0 and 6.0 μm are strong, as are the 4.27 μm $^{12}\text{C}=\text{O}$ stretch and the 15.3 μm O=C=O bending mode of CO_2 . The $^{13}\text{C}=\text{O}$ stretch of CO at 4.67 μm is clearly detected. The absorption band around 7 μm , attributed to solid CH_4 (Boogert et al. 1996, 1997) is present as well. The unidentified absorption feature around 6.8 μm , also observed toward NGC 7538 IRS9 and RAFGL 7009S (Schutte et al. 1996; d’Hendecourt et al. 1996) is also present in Cep A. The 9.7 μm amorphous silicate feature consists of a very deep, saturated, absorption. From the non-saturated wings of this feature we can again derive a visual extinction, resulting in a value of $A_V = 270^{m.}$ for Cep A East. This value is within the range of $A_V = 75\text{--}1000^{m.}$ extinction for the central source and nebula reported by Lenzen et al. (1984). PAHs appear absent in Cep A East.

From the integrated optical depth $\int \tau(\nu) d\nu$ of a non-saturated absorption feature we can compute a column density N using an intrinsic band strength A_m . For H_2O , CO, CO_2 and CH_4 ices, values of A_m were measured by Gerakines et al. (1995) and Boogert et al. (1997). For silicates, A_m is taken from Tielens & Allamandola (1987), based on the lab measurements by Day (1979). Integrated optical depth and column density values are listed in Table 2. The derived abundances of 100:6:15 for

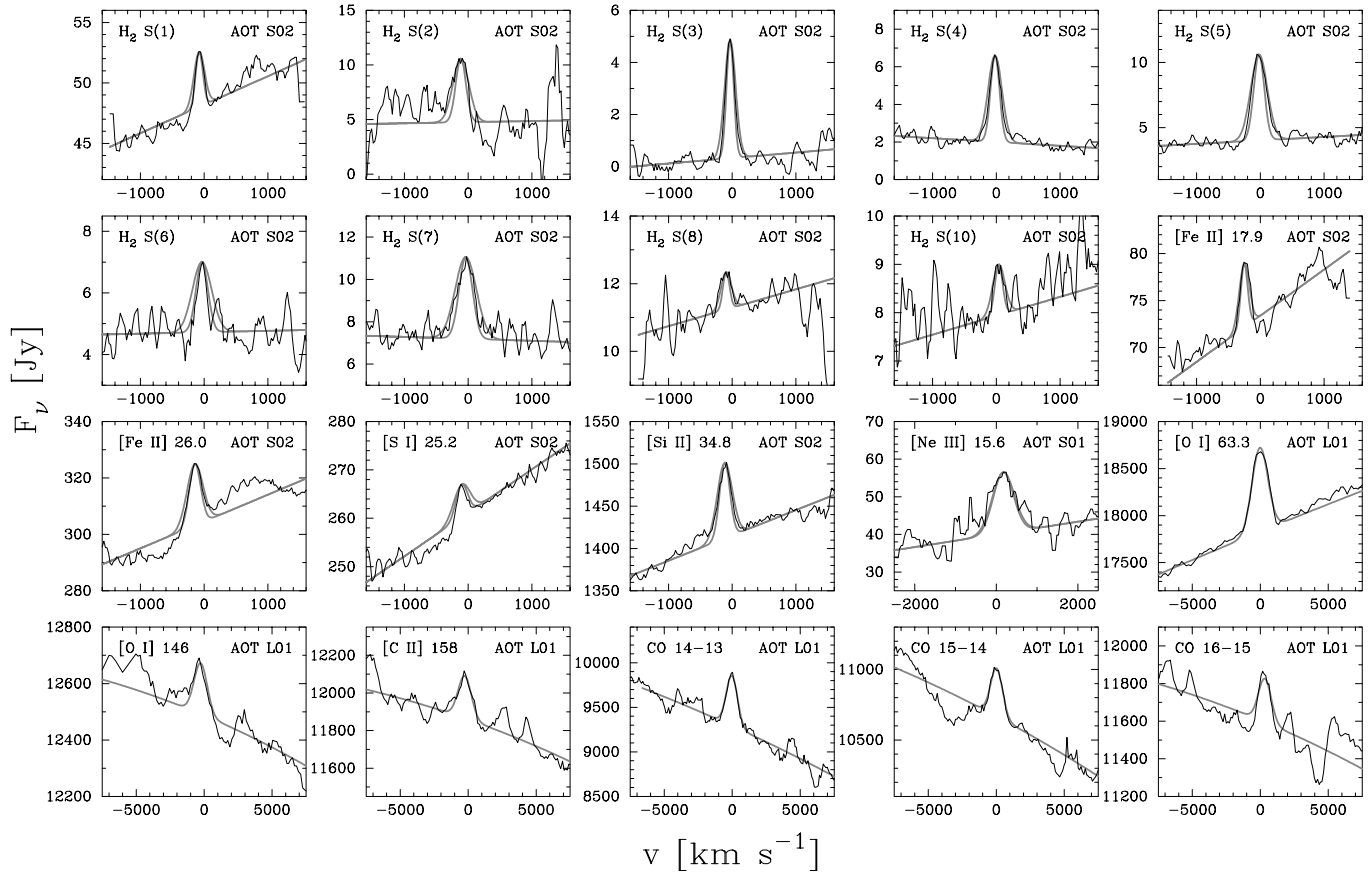


Fig. 6. Same as Fig. 5 for Cep A East.

H₂O:CO:CO₂ in Cep A East are within the range of values observed in other lines of sight (Whittet et al. 1996; d’Hendecourt et al. 1996).

4. Hydrogen recombination lines

A rich spectrum of H I recombination lines is present in the SWS data of S106 (Table 1). In contrast, H I lines are absent from the infrared spectra of Cep A East. It is not clear whether the H I lines observed with the rather large ($27'' \times 14''$) SWS beam in S106 are dominated by the strong ($\dot{M} \simeq 10^{-5} M_{\odot} \text{ yr}^{-1}$) stellar wind (Hippelein & Münch 1981; Felli et al. 1984), or could be due to the extended H II region seen in H α and Br γ (Bally et al. 1998; Hayashi et al. 1990; Greene & Rayner 1994; Maillard et al. 1999).

A clue to what is the case could come from the observed line profiles. As can be seen from Fig. 5, the H I lines observed in S106 are wider than the instrumental line profile for a point source. Unfortunately, the effect of line broadening of a compact source with FWHM of a few hundred km s⁻¹, as expected for the stellar wind (Felli et al. 1985; Drew et al. 1993), would be about the same as that of observing narrow recombination lines from an extended H II region. However, from the fact that our Br α line flux of $1.7 \times 10^{-14} \text{ W m}^{-2}$ is identical to that observed by other authors in smaller apertures (Garden & Geballe 1986; Persson et al. 1988; Drew et al. 1993), we conclude that at least

for Br α the dominant component must be the compact wind. In view of the limited spectral resolution of our data, a full analysis of the wind structure is beyond the scope of the present paper.

5. Molecular hydrogen emission

Both S106 and Cep A East are well-known sources of extended molecular hydrogen emission (Longmore et al. 1986; Hayashi et al. 1990; Bally & Lane 1982; Doyon & Nadeau 1988; Goetz et al. 1998). All ground-based H₂ measurements in literature refer to the ro-vibrational transitions, with upper energy levels $E(J)/k$ above 5000 K. These do not probe the bulk of the H₂, which is expected to be at much lower temperatures. However, in both S106 and Cep A East we have detected many pure rotational lines of H₂ (Table 1), which have much lower upper energy levels and are therefore able to directly probe the physical conditions in the dominant chemical species. And since their transition probabilities are quite small, these lines are optically thin and the excitation temperature will be close to the kinetic temperature of the gas.

From the H₂ line fluxes $I(J)$ listed in Table 1 it is possible to calculate the apparent column densities of molecular hydrogen in the upper J levels, averaged over the SWS beam, $N(J)$, using $N(J) = \frac{4\pi I(J)}{A} \frac{\lambda}{hc}$, with λ the wavelength, h Planck’s constant and c the speed of light. The transition probabilities A were taken from Turner et al. (1977). Line fluxes were corrected for

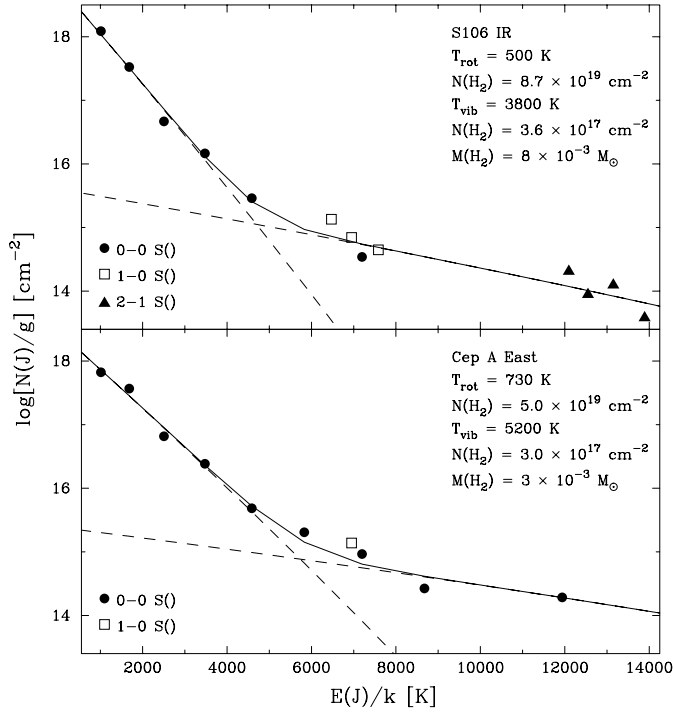


Fig. 7. H_2 excitation diagrams for S106 (top) and Cep A East (bottom). ISO observations of pure rotational lines are indicated by the circles. Triangles and squares indicate ground-based measurements of ro-vibrational lines from literature. The dashed lines give the Boltzmann distribution fits to the low-lying pure rotational lines and all lines with upper level energies above 5000 K. The solid line shows the sum of both contributions.

extinction using the average interstellar extinction law by Fluks et al. (1994). For S106 IR we adopted the value of $A_V = 13^m7$ derived in Sect. 3. The fact that the 0–0 S(3) line of H_2 , with a wavelength near the center of the $9.7 \mu\text{m}$ amorphous silicate feature, was detected in Cep A indicates that it cannot suffer from the same extinction as the continuum; the H_2 emission must originate in a spatially separate region from the continuum. Therefore we adopt a much smaller value of $A_V = 2^m$, expected to be a reasonable value for an origin in either a shock or PDR, for the emission lines observed toward Cep A East. Since the extinction correction at these mid-infrared wavelengths is small, a mis-estimate of A_V by a few magnitudes will not affect our results.

A useful representation of the H_2 data is to plot the log of $N(J)/g$, the apparent column density for a given J upper level divided by the statistical weight, versus the energy of the upper level, taken from Dabrowski (1984). These plots are shown in Fig. 7. Also plotted in these figures are several measurements of H_2 ro-vibrational lines in S106 and Cep A from literature (Longmore et al. 1986; Tanaka et al. 1989; Bally & Lane 1982). Although these measurements were taken at the same positions on the sky as ours, the beam sizes used were different and hence one may expect to see systematic differences in the derived specific intensities if the source of H_2 radiation is more extended than the beam size. In fact only the S106 measurements by Long-

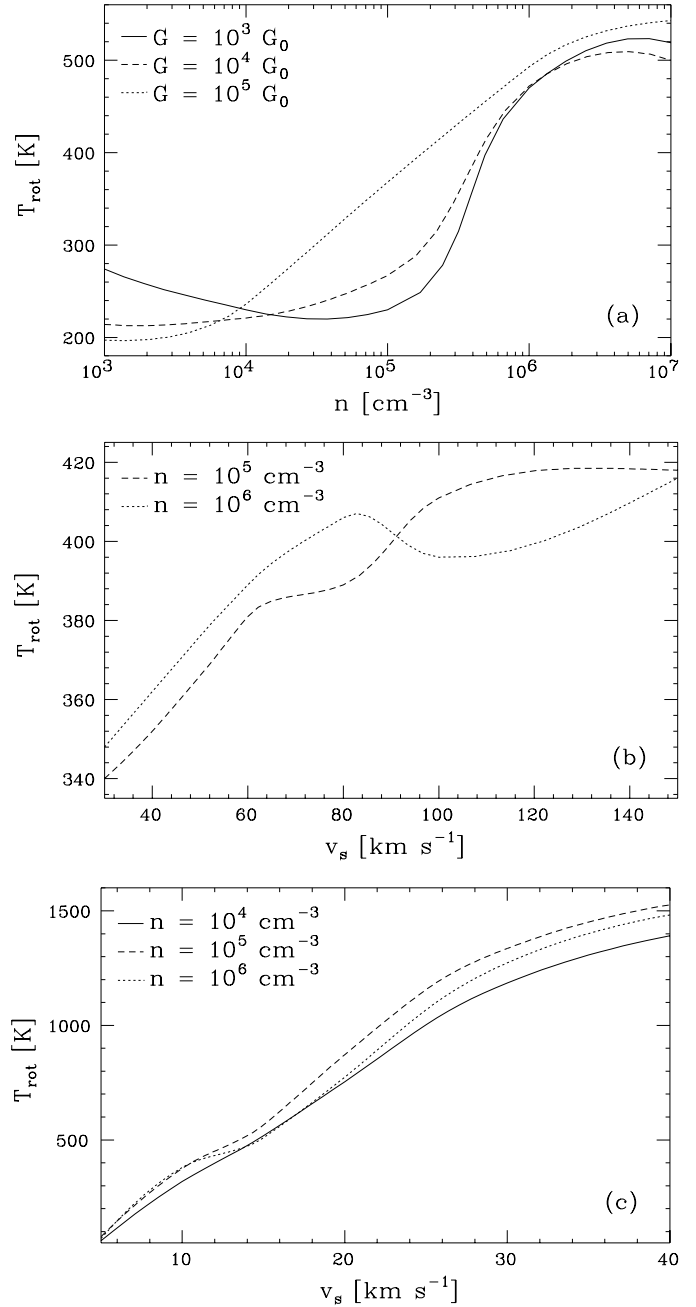


Fig. 8a–c. Theoretical relation between **a** $T_{\text{rot}}(\text{H}_2)$ and n for PDR models, **b** $T_{\text{rot}}(\text{H}_2)$ and v_s for J-shock models, and **c** $T_{\text{rot}}(\text{H}_2)$ and v_s for C-shock models.

more et al. (1986), taken with the smallest beam diameter, $12''$, differ systematically from the other measurements, indicating that the extent of the H_2 emitting region in S106 is probably somewhat larger than their beam size. This agrees well with H_2 1–0 S(1) images of the region (Hayashi et al. 1990; Maillard et al. 1999). In Fig. 7 the Longmore et al. measurements of S106 were scaled to the Tanaka et al. data.

The statistical weight g used in Fig. 7 is a combination of the rotational and nuclear spin components. We have assumed the high temperature equilibrium relative abundances of 3:1 for the

ortho and para forms of H_2 (Burton et al. 1992). For a Boltzmann distribution, the points in the plot shown in Fig. 7 should form a nearly straight line whose slope is inversely proportional to the excitation temperature, while its intercept is a measure of the total column density of warm gas. Using the formula by Parmar et al. (1991) and the rotational constants by Dabrowski (1984) to fit our data points in the low-lying pure rotational levels to a Boltzmann distribution, we arrive at values of 500 K and $9 \times 10^{19} \text{ cm}^{-2}$ and 730 K and $5 \times 10^{19} \text{ cm}^{-2}$ for S106 IR and Cep A East, respectively. Using the distances to S106 and Cep A of 1200 and 690 pc (Rayner 1994; Mel'nikov et al. 1995), this corresponds to total molecular hydrogen masses of 0.008 and $0.003 M_\odot$ within the SWS beam. Using the alternative distance estimate towards S106 of 600 pc (Staudte et al. 1982) would decrease the S106 H_2 mass to $0.004 M_\odot$. The fitted Boltzmann distributions are shown as the leftmost dashed lines in Fig. 7. The fact that the points for the ortho and para form of H_2 lie on the same line proves that our assumption on their relative abundances is correct.

As can be seen from Fig. 7, both the pure-rotational and ro-vibrational lines of H_2 with upper level energies higher than 5000 K deviate significantly from the leftmost dashed line. In both cases a Boltzmann distribution was fitted to these lines as well, shown as the rightmost dashed line in both figures. In the case of S106, the relative location of the 1–0 and 2–1 S(1)-lines in Fig. 7 are indicative of fluorescent excitation through UV pumping (Draine & Bertoldi 1996; Black & van Dishoeck 1987). The fitted Boltzmann distribution to the higher energy levels has thus no physical meaning, but may still be useful to provide a simple parametrization of the relative population of the energy levels. In the case of Cep A, the lines may indicate the presence of a smaller column ($3 \times 10^{17} \text{ cm}^{-2}$) of hot (a few 1000 K) molecular hydrogen, in addition to the large column of warm gas.

Employing predictions of H_2 emission from PDR, J-shock and C-shock models by Burton et al. (1992), Hollenbach & McKee (1989) and Kaufman & Neufeld (1996), we determined the excitation temperature T_{rot} from the low-lying pure rotational levels from these models as a function of density n and either incident FUV flux G (in units of the average interstellar FUV field $G_0 = 1.2 \times 10^{-4} \text{ erg cm}^{-2} \text{ s}^{-1} \text{ sr}^{-1}$; Habing 1968) or shock velocity v_s in an identical way as was done for the observations. The resulting relations between T_{rot} and n or v_s are shown in Fig. 8. As can be seen from these plots, the PDR and J-shock models predict a fairly small (200–540 K) range of resulting excitation temperatures, whereas in the C-shocks this range is much larger (100–1500 K). Furthermore, we see that in the model predictions for shocks the resulting T_{rot} does not depend much on density, whereas for PDRs it does not depend much on G , suggesting that once the mechanism of the H_2 emission is established, it can be used to constrain v_s or n in a straightforward way.

Comparing the excitation temperatures of 500 and 730 K for S106 and Cep A with those plotted in Fig. 8, we note that for S106 this falls well within the range of PDR- and C-shock model predictions, but are too high compared to the ones expected

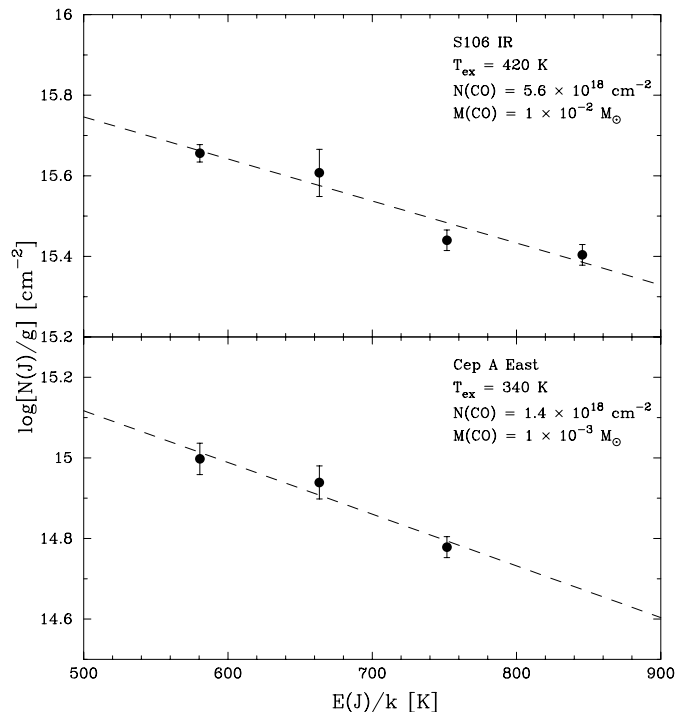


Fig. 9. CO excitation diagrams for S106 (top) and Cep A East (bottom). The dashed lines give the fits of the Boltzmann distribution to the data points.

from J-shocks. The observed bright PAH emission features (Sect. 3) and the atomic fine-structure line spectrum (Sect. 6) point towards a PDR origin for the H_2 emission in S106. The higher temperature for Cep A can only be reproduced by the C-shock models. Therefore we tentatively conclude that a dense ($\geq 10^6 \text{ cm}^{-3}$) PDR seems to be the best candidate to explain the observed H_2 emission in S106 IR and a slow ($\approx 20 \text{ km s}^{-1}$) non-dissociative shock can explain the observed warm column of H_2 in Cep A East. Since the regions we are looking at probably only fill part of the SWS beam, the absolute intensity of the H_2 emission listed in Table 1 can also be reproduced by these same models by varying the beam filling factor.

6. Carbon-monoxide emission lines

In both S106 IR and Cep A East several ro-vibrational emission lines due to gas-phase CO were detected in the long-wavelength part of the LWS spectra (Figs. 5 and 6). Similar to what was done for the H_2 emission in the previous section, we constructed CO excitation diagrams, using molecular data from Kirby-Docken & Liu (1978). They are shown in Fig. 9. The temperature and column of CO resulting from the Boltzmann fit to this excitation diagram are 420 K and $5.6 \times 10^{18} \text{ cm}^{-2}$ and 340 K and $1.4 \times 10^{18} \text{ cm}^{-2}$ for S106 and Cep A East, respectively. Corresponding CO masses are $1 \times 10^{-2} M_\odot$ (S106 at 1200 pc; for the 600 pc distance estimate this mass estimate would decrease to $3 \times 10^{-3} M_\odot$) and $1 \times 10^{-3} M_\odot$ (Cep A East).

The CO excitation temperature of 420 K for S106 is somewhat lower than that found from the H_2 lines, in agreement

with what is expected from a PDR, in which the CO emission arises in deeper embedded regions than the H₂. We conclude that a PDR is the most likely candidate for the source of the gas-phase CO emission in S106. For Cep A East the CO excitation temperature of 340 K is much lower than that found from the H₂ lines. This behaviour is hard to reconcile with an origin in the C-shock invoked to explain the H₂ observations. However, a J-shock, necessary to explain the ionic lines which we will discuss in the next section, may produce the observed CO emission while only emitting little warm H₂. Since the LWS CO observations were made with a much larger beam than the SWS H₂ observations, an alternative explanation may be that we are observing emission from two spatially distinct regions. The relatively large mass of warm CO as compared to that seen in H₂ may also easily be explained in this scenario.

The observed CO lines have critical densities of around 10^6 cm^{-3} . Therefore the detection of these lines also implies densities of this order of magnitude or higher in the originating region. For the shock seen in Cep A East this may not be unreasonable. However, assuming that these densities would exist in the entire S106 PDR would be implausible. If these CO lines do indeed arise in the large-scale environment of S106, the PDR must therefore have a clumpy structure (e.g. Burton et al. 1990). An alternative explanation of the presence of these lines, would be to identify the originating region with the surface of the extended disk-like structure surrounding S106 which could act like a PDR. With the present data-set we cannot make a distinction between these two possibilities.

7. Atomic fine structure lines

Important constraints on the physical conditions in the line emitting region come from the observed fine structure lines. As a first step towards identifying the mechanism responsible for the observed emission we can look at the mere presence of certain lines. The observed lines with high ionization potentials in S106, such as [O III], [Ar III], [Ne III], [Ni III], [Fe III] and [S IV] can only originate in the H II region surrounding S106. The PAH emission as well as the molecular lines observed towards S106 are indicative of the presence of a PDR as well. This PDR might contribute to the observed [Fe II], [Ni II], [Si II], [O I] and [C II] emission. We thus need to model the fine-structure lines in S106 IR as arising in the combination of an H II model and a PDR.

We have used the photo-ionization code CLOUDY (version 90.04; Ferland 1996) to generate model predictions for line strengths for the H II region surrounding S106 IR, assuming a spherical geometry and constant hydrogen density throughout the region. We generated a grid of models in which the input spectrum, taken from Kurucz (1991) models for a stellar photosphere, and the electron density in the H II region were varied. The total luminosity of the model was fixed to the total bolometric luminosity of S106 of $4.2 \times 10^4 L_{\odot}$ (computed from the spectral energy distribution using data from literature and assuming a distance of 1.2 kpc). The line ratios of the observed [O III] and [S III] fine structure lines are expected to depend mainly on density, and hardly on the temperature. Their be-

haviour in our H II region model together with the observed line ratios in S106 are shown in Fig. 10. From the fact that both line ratios agree on the thus obtained value for the electron density in the H II region, $1.3\text{--}2.5 \times 10^3 \text{ cm}^{-3}$, we conclude that our assumption of a constant density is reasonable.

Several other lines ratios ([Ar II]/[Ar III], [Ne II]/[Ne III] and [S III]/[S IV]) depend mainly on the effective temperature of the star and do not depend on density much. Their behaviour in the CLOUDY models for S106 is shown in Fig. 10 as well. From these plots, it can be seen that the source of ionizing photons should have a temperature between 37,000 and 40,000 K, corresponding to a spectral type of O6–O8, in good agreement with earlier determinations (Gehrz et al. 1982; Staude et al. 1982). However, not all observed line ratios yield the same temperature for the central star. Most likely this is due to the fact that the Kurucz models used for the input spectrum do not include the opacity shortward of the He II ionization limit due to the stellar wind, which is expected to be strong in the case of S106. The true temperature for the central source is therefore expected to be around the lower range of temperatures deduced from the Kurucz synthetic photospheres, i.e. around 37,000 K. For illustrative purposes, we also show the ratio of [O I] 63.2 μm /[O III] 51.8 μm for our model H II region, showing that virtually all the atomic oxygen will be in the form of [O III] and that we can thus safely attribute all of the observed [O I] emission to the PDR.

To be able to explain the observed intensity of $1.3 \times 10^{-2} \text{ erg s}^{-1} \text{ cm}^{-1} \text{ sr}^{-1}$ for the [Si II] line at 34.8 μm in S106, the Tielens & Hollenbach (1985) PDR models require a density higher than $\approx 10^5 \text{ cm}^{-3}$ and $G \geq 10^5 G_0$. This regime can also reproduce the observed ratios of [Si II] and the [Fe II] and [O I] lines, although to reproduce both the exact strength of the [Si II] emission and the relative strength to that of the [Fe II] lines requires a [Fe II] depletion of $\approx 30\%$ higher than the one assumed in the Tielens & Hollenbach models. An alternative explanation could be that the PDR doesn't fill the SWS aperture at 35 micrometer ($33'' \times 20''$) completely, increasing the surface brightness of all lines. The predicted intensities of [S I] and [Fe I] are sufficiently low to be undetectable, in agreement with the observations.

Towards Cep A East, only fine structure lines that can be produced in shocks were observed. In contrast to both C- and J-shocks, PDRs do not produce significant quantities of [S I] emission (Tielens & Hollenbach 1985). Therefore this line must be completely due to one or more shocks. C-shocks only contain trace fractions of ions and hence cannot explain the observed [Fe II], [Si II] and [C II] emission. Hence the simplest hypothesis would be to try to explain the observed fine-structure lines in Cep A in terms of a J-shock model. To explain the [S I] surface brightness of $1.0 \times 10^{-3} \text{ erg s}^{-1} \text{ cm}^{-2} \text{ sr}^{-1}$ requires a moderately dense ($10^4\text{--}10^5 \text{ cm}^{-3}$) pre-shock gas. If the shock does not fill the ISO beam completely, as is expected, this number will go up. The absence of [Fe I] emission does indicate that we are dealing with higher ($10^5\text{--}10^6 \text{ cm}^{-3}$) densities, so line ratios seem to provide more reliable constraints in this case. However, the aperture sizes for lines measured at different wavelengths are also different in some cases, making this method only re-

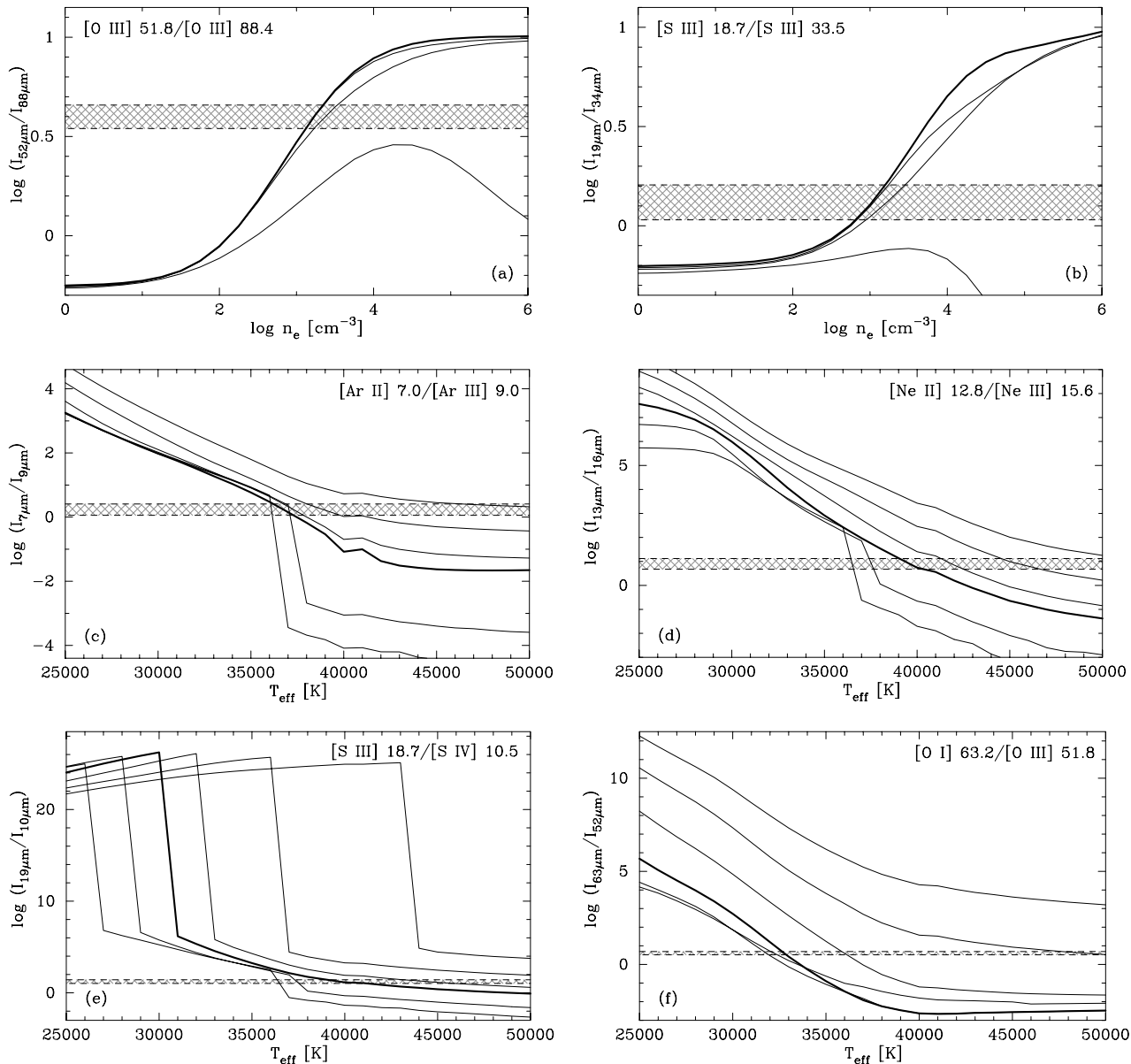


Fig. 10a–f. CLOUDY model predictions for various emission line ratios from the S106 H II region as function of electron density n_e and temperature of the ionizing star. The hatched regions between the dashed lines show the error interval of the observed ratios in S106 IR. The solid lines show the computed ratios for $\log n_e = 1.0\text{--}6.0$, or $T_{\text{eff}} = 15,000\text{--}50,000$ K. The heavy curves indicate the lines with $\log n_e = 3.0$ or $T_{\text{eff}} = 40,000$ K (best fit). **a** Behaviour of the [O III] 51.8 μm /[O III] 88.4 μm line flux ratio. **b** The same for the [S III] 18.7 μm /[S III] 33.5 μm ratio. **c** Same for the [Ar II] 7.0 μm /[Ar III] 9.0 μm ratio. **d** Same for the [Ne II] 12.8 μm /[Ne III] 15.6 μm ratio. **e** Same for the [S III] 18.7 μm /[S IV] 10.5 μm ratio. **f** Same for the [O I] 63.2 μm /[O III] 51.8 μm ratio.

liably applicable to line ratios measured in identical SWS or LWS apertures. Therefore the ratio of [Fe II] 26.0 μm to [S I] 25.2 μm might provide the most reliable indicator of physical conditions in the shock. To reproduce the observed value of 0.26 with the Hollenbach & McKee (1989) J-shock models requires either moderately dense (10^5 cm^{-3}) gas with a low (30 km s^{-1}) shock velocity or a high (10^6 cm^{-3}) density with a faster ($\approx 60 \text{ km s}^{-1}$) shock. To have the predicted [Fe I] emission sufficiently low to explain our non-detections of this species, the

moderately dense, slow J-shock model is required. This regime also reproduces the relative [Si II] strength.

As was discussed in the previous section, one or multiple J-shocks cannot reproduce the observed H₂ emission (although a contribution to this can be expected). The success of the J-shock model in explaining the observed fine-structure lines and the absence of PAH emission in Cep A East, excluding the possibility of a significant contribution from a PDR, leads us to pose that a combination of one or more J- and C-shocks must be responsible for the observed emission in Cep A. The presence of more

than one type of shock in the region could be linked to the reported multiple episodes of outflow activity from the embedded source (Narayanan & Walker 1996). In the presence of both a J- and a C-shock, the [Si II] and [Fe II] emission would originate completely in the J-shock, whereas both the C- and the J-shock would contribute to the observed [S I] and H₂ spectra. With the J-shock parameters derived from the fine-structure lines, an additional C-shock component with a shock-velocity of about 20 km s⁻¹ is required to reproduce the observed pure rotational H₂ emission. The observed hot column of H₂ in Cep A may then be due to formation pumping (the effect that H₂ gets reformed with non-zero energy in the post-shock gas after being dissociated in the shock front) in the J-shock. To have the rovibrational lines of comparable intensity as the rotational lines (through collisional excitation) requires pre-shock densities of the order of 10⁶ cm⁻³. For both S106 IR and Cep A, predicted lines strengths of the best fit models are also listed in Table 1.

8. Discussion and conclusions

In the previous sections we saw that the infrared emission-line spectrum of S106 could be well explained by the presence of an H II region and a clumpy PDR. The average density in the H II region should be around 2×10^3 cm⁻³. The density in the PDR, which was estimated to be 10⁵–10⁶ cm⁻³, is several orders of magnitude higher, in agreement with one would expect in a scenario in which a young massive star has photo-ionized its natal cloud in all but the densest clumps.

In Sect. 7 we concluded that the incident FUV flux on the S106 PDR should be rather high ($\geq 10^5$ G₀). We also showed that the central source in S106 is of spectral type O8, with a total luminosity of 4.2×10^4 L_⊙. From a Kurucz (1991) model for a stellar photosphere with $T_{\text{eff}} = 37,000$ K and $\log g = 4.0$, we compute that such a star emits a total FUV (6–13.6 eV) flux of 3.6×10^{36} erg s⁻¹ sr⁻¹. To dilute this stellar FUV field to a value of 10⁵–10⁶ G₀, the PDR must be at a location 3–10 × 10³ AU away from the central star, corresponding to a projected distance of 5–17". This projected distance is independent of the assumed distance towards S106. It is within the range allowed by the SWS entrance apertures and is compatible with an origin in the $\approx 30''$ diameter region of H₂ emission in the H₂ 1–0 S(1) image of S106 by Hayashi et al. (1990). We conclude that a central O8 star is sufficient to produce the FUV radiation field reaching the S106 PDR.

These results agree well with other determinations. Schneider et al. (2000) have spatially resolved the 157.7 μm [C II] and 63.2 μm [O I] emission in S106 and concluded that there is a PDR region with density $\simeq 10^6$ cm⁻³ and strong (up to 8×10^5 G₀) UV field in the immediate environment of S106 and a more extended dense (10⁵–10⁶ G₀) PDR region exposed to a lower intensity (300–500 G₀) UV field. We are clearly dominated by their first component. This same component may be identified with the high-density (10⁵ cm⁻³) fluorescent H₂ regions identified by Hayashi et al. (1990).

Both the presence of [S I] 25.2 μm emission and the H₂ spectrum point unambiguously to shocked gas as the origin of

the infrared emission lines in Cep A East. A combination of a slow (20 km s⁻¹) non-dissociative shock and a faster (30–60 km s⁻¹) dissociative shock are required to explain our ISO spectra. The density of the pre-shock gas in Cep A East is similar to that in the S106 PDR: 10⁵–10⁶ cm⁻³. Our J-shock component may be identified with the [Fe II] 1.64 μm clumps observed by Goetz et al. (1998). The C-shocks could be due to their H₂ knots which do not show ionic emission.

It is interesting to compare the results derived here for the emission from the eastern lobe of Cep A with the results by Wright et al. (1996), obtained using the same instruments on board ISO, for the western part of the nebula. They derived a T_{rot} of 700 ± 30 K for the H₂ lines with upper level energies up to 7000 K, and a temperature range up to 11,000 K for the higher upper level energies. They explained this H₂ emission as arising from a combination of at least two C-shocks with different pre-shock density, shock velocity and covering factor. In addition to this, they also reported emission from [Ne II], [S I] and [Si II], which they explained as arising in a planar J-shock with pre-shock density of 10³–10⁴ cm⁻³ and shock velocity 70–80 km s⁻¹. Qualitatively, the detected lines in the eastern and western part of the nebula are well in agreement. The main difference between the observed lines seems to be that they are much more intense in the western part of Cep A, indicating that the densities there are a factor of 100 higher than those obtained for the eastern lobe, but the shock velocities are comparable in both parts of the nebula. The similarity between these two parts of Cep A are in agreement with a scenario in which the driving source of the molecular outflow, HW-2, went through multiple episodes of outflow activity, as suggested by Narayanan & Walker (1996). In this scenario, the J-shock component could be due to the most recent period of enhanced mass loss, whereas one or more C-shocks could be due to older generations of outflows. Alternatively, the stellar wind material could produce a (fast) J-shock while the surrounding molecular cloud might be swept up by a slower C-shock.

As was already remarked by Staude & Elsässer (1993), the differences between the environments of these two massive embedded YSOs, S106 and Cep A, are remarkable. The mid- and far-infrared observations presented in this paper show that the difference between these two sources cannot be due to a different orientation of their nebulae; it can only be a reflection of their different evolutionary status, with Cep A being the younger of the two. In S106 the stellar wind and UV radiation of the exciting source have cleared and excited a sufficiently large region to create strong PDR emission, whereas in the case of Cep A, the central source is still heavily embedded and we only observe the interaction of the outflow with its surroundings. In due time, Cep A will clear its surroundings, ionize the hydrogen, and evolve into a bipolar nebula quite similar to S106.

Acknowledgements. The authors would like to thank John Rayner and Klaus-Werner Hodapp for providing us with the K-band images of S106 and Cep A shown in Figs. 1 and 2. Peter van Hoof is kindly acknowledged for providing us with a copy of the CLOUDY computer code. Frank Molster is thanked for providing the authors with valuable input on a draft of the paper. MvdA acknowledges financial support

from NWO grant 614.41.003 and through a NWO *Pionier* grant to L.B.F.M. Waters. This research has made use of the Simbad data base, operated at CDS, Strasbourg, France.

References

- Alonso-Costa J.L., Kwan J., 1989, *ApJ* 338, 403
 Bally J., Lane A.J., 1982, *ApJ* 257, 612
 Bally J., Yu K.C., Rayner J., Zinnecker H., 1998, *AJ* 116, 1868
 Bieging J.H., 1984, *ApJ* 286, 591
 Black J.H., van Dishoeck E.F., 1987, *ApJ* 322, 412
 Boogert A.C.A., Schutte W.A., Tielens A.G.G.M., et al., 1996, *A&A* 315, L377
 Boogert A.C.A., Schutte W.A., Helmich F.P., et al., 1997, *A&A* 317, 929
 Burton M.G., Hollenbach D.J., Tielens A.G.G.M., 1990, *ApJ* 365, 620
 Burton M.G., Hollenbach D.J., Tielens A.G.G.M., 1992, *ApJ* 399, 563
 Casement L.S., McLean I.S., 1996, *ApJ* 462, 797
 Cesarsky D., Lequeux J., Abergel A., et al., 1996, *A&A* 315, L309
 Chernoff D.F., Hollenbach D.J., McKee C.F. 1982, *ApJ* 259, L97
 Clegg P.E., Ade P.A.R., Armand C., et al., 1996, *A&A* 315, L38
 Dabrowski I., 1984, *Canadian J. Phys.* 62, 1639
 Day K.L., 1979, *ApJ* 234, 158
 de Graauw Th., Haser L.N., Beintema D.A., et al., 1996, *A&A* 315, L49
 d'Hendecourt L., Jourdain de Muizon M., Dartois A., et al., 1996, *A&A* 315, L365
 Doyon R., Nadeau D., 1988, *ApJ* 334, 883
 Draine B.T., Bertoldi F., 1996, *ApJ* 468, 269
 Drew J.E., Bunn J.C., Hoare M.G., 1993, *MNRAS* 265, 12
 Eiroa C., Elsässer H., Lahulla J.F., 1979, *A&A* 74, 89
 Ellis H.B., Lester D.F., Harvey P.M., et al., 1990, *ApJ* 365, 287
 Evans N.J., Becklin E.E., Beichman C., et al., 1981, *ApJ* 244, 115
 Felli M., Staude H.J., Reddman T., et al., 1984, *A&A* 135, 261
 Felli M., Simon M., Fischer J., Hamann F., 1985, *A&A* 145, 305
 Ferland G.J., 1996, Univ. of Kentucky Physics Department Internal Report
 Fluks M.A., Plez B., Thé P.S., et al., 1994, *A&AS* 105, 311
 Garden R.P., Geballe T.R., 1986, *MNRAS* 220, 611
 Geballe T.R., Lacy J.H., Persson S.E., McGregor P.J., Soifer B.T., 1985, *ApJ* 292, 500
 Gehrz R.D., Grasdalen G.L., Castelaz M., et al., 1982, *ApJ* 254, 550
 Gerakines P.A., Schutte W.A., Greenberg J.M., van Dishoeck E.F., 1995, *A&A* 296, 810
 Goetz J.A., Pipher J.L., Forrest W.J., et al., 1998, *ApJ* 504, 359
 Greene T.P., Rayner J.T., 1994, In: McLean I. (ed.) *Astronomy with Infrared Arrays*, Kluwer Academic Publishers, p. 453
 Habing H.J., 1968, *Bull. Astron. Inst. Netherlands* 19, 421
 Hartigan P., Carpenter J.M., Dougados C., Skrutskie M.F., 1996, *AJ* 111, 1278
 Hayashi S.S., Hasegawa T., Tanaka M., et al., 1990, *ApJ* 354, 242
 Hefele H., Hölzle E., 1980, *A&A* 88, 145
 Hippelein H., Münch G., 1981, *A&A* 99, 248
 Hodapp K.W., 1994, *ApJS* 94, 615
 Hodapp K.W., Rayner J., 1991, *AJ* 102, 1108
 Hollenbach D.J., McKee C.F., 1989, *ApJ* 342, 306
 Hollenbach D.J., Tielens A.G.G.M., 1999, *Rev. Mod Phys.* 71, 173
 Hughes V.A., 1988, *ApJ* 383, 280
 Hughes V.A., Wouterloot J.G.A., 1984, *ApJ* 276, 204
 Kaufman M.J., Neufeld D.A., 1996, *ApJ* 456, 611
 Kessler M.F., Steinz J.A., Anderegg M.E., et al., 1996, *A&A* 315, L27
 Kirby-Docken K., Liu B., 1978, *ApJS* 36, 359
 Kurucz R.L., 1991, In: Davis Philip A.G., Uppgren A.R., Janes K.A. (eds.) *Stellar atmospheres—Beyond classical models*, Schenectady, New York: L. Davis press, p. 441
 Lenzen R., Hodapp K.W., Solf J., 1984, *A&A* 137, 202
 Longmore A.J., Robson E.I., Jameson R.F., 1986, *MNRAS* 221, 589
 Loushin R., Crutcher R.M., Bieging J.H., 1990, *ApJ* 362, L67
 Maillard J.P., Joblin C., Mitchell G.F., Vauglin I., Cox P., 1999, In: Cox P., Kessler M.F. (eds.) *The universe as seen by ISO*, ESA SP-427, p. 707.
 Mel'nikov S.Y., Shevchenko V.S., Grankin K.N., 1995, *Astron. Rep.* 39, 42
 Mezger P.G., Chini R., Kreysa E., Wink J., 1987, *A&A* 182, 127
 Narayanan G., Walker C.F., 1996, *ApJ* 466, 844
 Parmar P.S., Lacy J.H., Achtermann J.M., 1991, *ApJ* 372, L25
 Persson S.E., McGregor P.J., Campbell B., 1988, *ApJ* 326, 339
 Pipher J.L., Sharpless S., Savedoff M.P., et al., 1976, *A&A* 51, 255
 Rayner J., 1994, In: McLean I.S. (ed.) *Infrared Astronomy with Arrays: The next generation*, Dordrecht: Kluwer, p. 185
 Schneider N., Kramer C., Simon R., 2000, In: Favata F., Kaas A.A., Wilson A. (eds.) *Proc. 33rd ESLAB Symposium "Star Formation from the Small to the Large Scale"*, ESA SP-445, in press
 Schutte W.A., Tielens A.G.G.M., Whittet D.C.B., et al., 1996, *A&A* 315, L333
 Staude H.J., Elsässer H., 1993, *Astron. Astroph. Rev.* 5, 165
 Staude H.J., Lenzen R., Dyck H.M., Schmidt G.D., 1982, *ApJ* 255, 95
 Tanaka M., Hasegawa T., Hayashi S.S., Brand P.W.J.L., Gatley I., 1989, *ApJ* 336, 207
 Tielens A.G.G.M., Allamandola L.J., 1987, In: Hollenbach D.J. Thronson Jr. H.A. (eds.) *Interstellar Processes*, Dordrecht: Reidel, p. 397
 Tielens A.G.G.M., Hollenbach D.J., 1985, *ApJ* 291, 722
 Turner J., Kirby-Docken K., Dalgarno A., 1977, *ApJS* 35, 281
 Whittet D.C.B., Schutte W.A., Tielens A.G.G.M., et al., 1996, *A&A* 315, L357
 Wright C.M., Drapatz S., Timmermann R., et al., 1996, *A&A* 315, L301